Arbitrary-order Hilbert Spectral Analysis and Intermittency in Solar Wind Density Fluctuations

Francesco Carbone[1] , Luca Sorriso-Valvo[2] , Tommaso Alberti[3] , Fabio Lepreti[3] , Christopher H. K. Chen[4], Zdenek Němeček[5] , and Jana Šafránková[5]

[1] CNR–Institute of Atmospheric Pollution Research, Division of Rende, UNICAL-Polifunzionale, I-87036 Rende (CS), Italy
francesco.carbone42@gmail.com, f.carbone@iia.cnr.it
[2] CNR–Nanotec, U.O.S. di Rende, ponte P. Bucci, cubo 31C, I-87036 Rende (CS), Italy
[3] Dipartimento di Fisica, Universitá della Calabria, Ponte P. Bucci, cubo 31C, I-87036 Rende, Italy
[4] School of Physics and Astronomy, Queen Mary University of London, London E1 4NS, UK
[5] Faculty of Mathematics and Physics, Charles University, Prague 18000, Czech Republic

Abstract

The properties of inertial- and kinetic-range solar wind turbulence have been investigated with the arbitrary-order Hilbert spectral analysis method, applied to high-resolution density measurements. Due to the small sample size and to the presence of strong nonstationary behavior and large-scale structures, the classical analysis in terms of structure functions may prove to be unsuccessful in detecting the power-law behavior in the inertial range, and may underestimate the scaling exponents. However, the Hilbert spectral method provides an optimal estimation of the scaling exponents, which have been found to be close to those for velocity fluctuations in fully developed hydrodynamic turbulence. At smaller scales, below the proton gyroscale, the system loses its intermittent multiscaling properties and converges to a monofractal process. The resulting scaling exponents, obtained at small scales, are in good agreement with those of classical fractional Brownian motion, indicating a long-term memory in the process, and the absence of correlations around the spectral-break scale. These results provide important constraints on models of kinetic-range turbulence in the solar wind.

Key words: plasmas – solar wind – turbulence

1. Introduction

The solar wind is a continuous flow of plasma expanding from the solar corona into interplanetary space. Almost 60 years after the first spacecraft measurements, our knowledge of solar wind phenomena has largely advanced, but many aspects of the fundamental processes are still not understood. Among these, the properties of turbulence and its role in the non-adiabatic expansion of the solar wind constitute one of the major research goals for the community (Bruno & Carbone 2013). Power-law spectra of velocity, magnetic field, and density fluctuations have long been observed throughout the heliosphere, and represent a robust characteristic of solar wind turbulence (Bruno & Carbone 2013). Unlike neutral fluid turbulence, the weakly collisional nature of solar wind plasma results in the presence of several scaling ranges. At scales larger than a few hours, the large-scale structure of the solar wind, probably of solar origin, generates a spectral region of energy input that can also display $E(\nu) \sim \nu^{-1}$ scaling (Bruno & Carbone 2013), where ν is the frequency measured in the spacecraft frame, and is characterized by mostly uncorrelated fluctuations. In the range between a few hours and a few seconds, the solar wind behaves as a magnetized flow and follows similar prescriptions to the classical Kolmogorov picture of inertial-range turbulence (Kolmogorov 1941). Various adaptations of the Kolmogorov phenomenology to MHD turbulence have been proposed (Iroshnikov 1964; Kraichnan 1965; Goldreich & Sridhar 1995; Boldyrev 2006), and the solar wind shows several properties that match these models, although aspects of these are still under debate. At smaller scales, the turbulence coexists with field–particle interactions (He et al. 2015), plasma instabilities, and other kinetic plasma processes. In this range, a steeper power-law spectrum is generally observed, whose nature is still under

investigation (Leamon et al. 1998; Alexandrova et al. 2008, 2013; Chen 2016; Consolini et al. 2017).

Among the characteristics of turbulence, inertial-range intermittency of velocity and magnetic field has been deeply studied in recent years (Bruno & Carbone 2013). Data analysis has shown that, as for neutral flows, the energy cascade is inhomogeneous, with the generation of localized small-scale structures that result in scale-dependent, non-Gaussian statistics of the field fluctuations (Marsch & Tu 1997; Sorriso-Valvo et al. 1999). The appropriate estimation of the degree of intermittency is important for determining the presence of energetic structures, such as vorticity filaments and current sheets, which are likely to play an important role in the dissipative and kinetic processes occurring in the small-scale range (Alexandrova et al. 2013). For example, numerical simulations have shown that magnetic reconnection may occur within current sheets (Servidio et al. 2012), and plasma instabilities are also mostly excited in the presence of these structures (Servidio et al. 2014). On the other hand, the presence of intermittency in the small-scale range is still not fully established, although most magnetic field observations seem to indicate self-similar, non-intermittent scaling in this range (Kiyani et al. 2009). However, different techniques have given different results (Alexandrova et al. 2008). This ambiguity needs to be resolved for a better constraint on the cascade and dissipative processes.

While most of the literature concerns the magnetic field fluctuations, some works have focused on the properties of density fluctuations. In particular, the turbulence and intermittency properties of density have been studied in the inertial range (Hnat et al. 2003; Chen et al. 2011; Bruno et al. 2014), and more recently at smaller scales (Chen et al. 2014;

Sorriso-Valvo et al. 2017). The analysis of *Spektr-R* data have shown the presence of two power-law frequency spectra $E(\nu) \propto \nu^{-\beta}$, separated by a break located around the proton gyroscale (Šafránková et al. 2013a, 2013b, 2015; Chen et al. 2014). In particular, a scaling typical of the inertial range, characterized by a power-law decay of the spectral density (with a slope $\beta \simeq 5/3$) is found at large scales, and steeper spectra with slopes in the range $\beta \simeq 1.76$–2.86 exist at smaller scales (Sorriso-Valvo et al. 2017). In the inertial range, the structure functions (SF) do not show proper scaling, so that the deviation from K41 (Kolmogorov 1941) was only evaluated through the standard multifractal analysis on a surrogate dissipation field (Sorriso-Valvo et al. 2017). As in the case of magnetic field, the determination of the presence of inter-mittency in the kinetic range is ambiguous, because different techniques resulted in different answers (Chen et al. 2014; Sorriso-Valvo et al. 2017). Indeed, the scaling exponents obtained through the SF analysis suggested a lack of intermittency (Chen et al. 2014), although they also showed some variability between intervals. Similar variability was also observed in the multifractal spectrum (Sorriso-Valvo et al. 2017), suggesting that further analysis is required to fully understand the properties of this small-scale dynamics. This ambiguity motivates the use of alternative techniques, in order to understand whether or not nonlinear correlations are generated also in this range of scales.

The difficulty in evaluating the presence of intermittency at small scales has several possible causes. First, the limited size of high-resolution samples causes possible effects due to poor statistical convergence, stationarity, or ergodicity. Second, the role of the inertial-range fluctuations may affect the statistical assessment of small-scale turbulence, because the presence of larger-scale structures (often in the form of ramp–cliff structures as also observed in the solar wind density; see for example the top panel of Figure 7) may lead, for example, to underestimation of the spectral index and of the SF scaling exponents. Ramp–cliff structures are a common features of scalar turbulence (Shraiman & Siggia 2000; Warhaft 2000) and have been observed in a variety of turbulent shear flows in both stably and unstably stratified conditions (Wroblewski et al. 2007). The typical pattern can be identified by a very rapid increase in the field (cliff) followed by a more gradual or smooth decrease (ramp), or vice versa (Sreenivasan 1991; Celani et al. 2000; Wroblewski et al. 2007). It is believed that the large-scale structures may non-locally couple with the small scales through the cliff structure (Yeung et al. 1995). Further-more, it has been shown that even the inertial-range scaling may be affected by the presence of large-scale periodic forcing structures (Huang et al. 2010). This may have a strong influence on both the small-scale and large-scale statistic-s (Huang et al. 2010, 2011). Ramp–cliff structures cannot be represented by a simple monochromatic component, and Fourier-based methods require high-order harmonic compo-nents to represent their difference. This leads to an asymptotic approximation process (Cohen 1995; Huang et al. 1998; Flandrin 1999), resulting in an artificial energy flux from the large to the small scales (Huang et al. 2011). As a result, the Fourier-based power spectrum is contaminated by this artificial energy flux, which is manifested as a shallower power spectrum (Huang et al. 2010). All these effects may be particularly important when the sample size is limited.

To correctly extract scaling information for solar wind proton density fluctuations, by minimizing the effect of the nonstationarity and the ramp–cliff structures embedded in the field, arbitrary-order Hilbert spectral analysis (HSA) (Huang et al. 2008, 2010; Carbone et al. 2016a) has been used in this work. HSA formally represents an extension of classical empirical mode decomposition (EMD), designed to character-ize scale-invariant properties directly in amplitude–frequency space (Huang et al. 2008). EMD was developed to process and analyze the temporal evolution of nonstationary data (Huang et al. 1998) and has been used in many different fields (Salisbury & Wimbush 2002; Vecchio et al. 2014; Carbone et al. 2016b; Alberti et al. 2017), including the analysis of high-resolution magnetic field data on the fast, quasi-stationary solar wind, as measured by the *Cluster* spacecraft (Consolini et al. 2017). The main advantage of EMD is that the basis functions are derived from the signal itself. Since EMD analysis is adaptive (in contrast to traditional decomposition methods where the basis functions are fixed) and not restricted to stationary data, the data set may be analyzed without introducing spurious harmonics or artifacts near sharp data transitions, which could appear when using classical Fourier filtering or high-order moments analysis. Indeed, EMD allows local information to be extracted through the instantaneous frequencies that cannot be captured by fixed-frequency methods (such as Fourier or wavelets). The main consequence is that the frequency is not widely spread (as for wavelets), with a much better frequency definition and smaller frequency modulation induced by amplitude variation (Huang et al. 1998; Liu et al. 2012).

2. Arbitrary-order HSA of Solar Wind Proton Density Data

In order to perform the arbitrary-order Hilbert analysis, the high-resolution solar wind proton density n_p (with a sampling period $\Delta t = 0.031$ s), measured by the BMSW instrument (Šafránková et al. 2013a) on the *Spektr-R* spacecraft, have been used (Šafránková et al. 2013a, 2013b, 2015; Chen et al. 2014; Sorriso-Valvo et al. 2017). All of the intervals were collected during the period 2011 November to 2012 August, and the total length of each interval is between 1 and 4 hr. In addition, the proton velocity v_p and temperature T_p were also sampled at the same frequency. The magnetic field B, not provided by *Spektr-R* instrumentation, was supplied by MFI on the *Wind* spacecraft, in the corresponding time interval (Chen et al. 2014), and was only used for estimating the typical plasma beta β_p of the intervals. All of the parameters are collected in Table 1. More details about the data can be found in Sorriso-Valvo et al. (2017). As is customary, the Taylor hypothesis is used to shift between time and space variables via the bulk solar wind speed, which is supersonic and super-Alfvénic for all intervals. In these conditions, the time series will be used as an instantaneous one-dimensional cut into the turbulent flow, so that all of the arguments in terms of space and wavevector will be given in terms of time and frequency, without loss of generality.

To apply HSA, the solar wind density measurements $n_p(t)$ were initially decomposed through classical EMD to obtain the intrinsic mode functions (IMFs), and the Hilbert transform was then applied to the IMFs. Within the EMD framework, the data are decomposed into a finite number k of oscillating basis functions $\phi_j(t)$, known as IMFs, characterized by an increasing timescale τ, and a residual $r_k(t)$ that describes the mean trend, if

Table 1
Main Parameters for the Eight Intervals

Interval	Date	Time	β_p	B	n_p	v_p
A	2011 Nov 10	15:55:40–18:46:55	0.78	4.7	4.6	370
B	2012 Jun 1	21:05:44–01:09:06	0.12	8.3	6.6	370
C	2012 Jun 2	02:34:52–03:26:43	0.17	9.1	7.9	360
D	2012 Jun 2	06:02:22–08:07:15	0.18	8.8	8.2	330
E	2012 Jul 9	08:25:56–11:09:51	0.06	12.0	6.0	400
F	2012 Jul 9	13:22:18–16:55:40	0.14	11.0	6.7	390
G	2012 Aug 9	10:48:52–15:59:13	0.74	4.7	4.0	320
H	2012 Aug 9	17:40:39–22:31:50	0.41	4.5	6.3	330

Note. Data are from *Spektr-R*, except *B*, which is from the upstream *Wind* spacecraft. The date refers to the initial time of the measurement. Time is in UT, magnetic field B in nT, the proton density n_p in cm^{-3}, and the proton speed v_p in km s^{-1}.

one exists, as

$$n_p(t) = \sum_{j=1}^{k} \phi_j(t) + r_k(t).$$ (1)

The decomposition consists of two stages: first, the local extrema of $n_p(t)$ are identified and subsequently connected through cubic spline interpolation. Once connected, the envelopes of local maxima and minima are obtained. Second, the mean $M_1(t)$ is calculated between the two envelope functions, then subtracted from the original data, $h_1(t) = n_p(t) - M_1(t)$. The difference $h_1(t)$ is an IMF only if it satisfies the following criteria: (i) the number of local extrema and zero-crossings does not differ by more than 1; (ii) at any point t, the mean value of the extrema envelopes is zero. When $h_1(t)$ does not meet these criteria, the sifting procedure is repeated using $h_1(t)$ as the new raw data series, and $h_{11}(t) = h_1(t) - M_{11}(t)$ is generated, where $M_{11}(t)$ is the mean of the envelopes. The sifting procedure is repeated m times until $h_{1m}(t)$ satisfies the above criteria. A general rule to stop the sifting is introduced by using a standard deviation σ, evaluated from two consecutive steps:

$$\sigma = \sum_{t=0}^{N} \frac{|h_{1(m-1)}(t) - h_{1m}(t)|^2}{h_{1(m-1)}^2(t)}.$$ (2)

The iterative process stops when σ is smaller than a threshold value σ_{thresh} (Huang et al. 1998; Cummings et al. 2004).

Since EMD acts intrinsically as a dyadic filter bank (Flandrin et al. 2004; Huang & Shen 2005), each IMF captures a narrow spectral band in frequency space (Huang et al. 2008, 2010; Carbone et al. 2016a) and their superposition behaves as $M(\nu) \equiv \max[\phi_j(\nu)] \sim \nu^{-\alpha}$. In Figure 1, the results of the EMD performed on interval A are reported. In both ranges, the behavior of $M(\nu)$ is compatible with the Fourier spectral indices: $\alpha \approx 1.66$ and $\alpha \approx 2.6$, for the inertial range and below the proton gyroscale respectively.

By comparison with the Fourier spectrum, each IMF can be interpreted according to its characteristic timescale. In particular, as is visible in Figure 1, modes 11–16 capture the dynamics of the MHD inertial range, while modes 2–6 capture the small-scale dynamics below the proton gyroscale. The intermediate range of scales, modes 7–10, do not show power-law scaling and are representative of the dynamics across the
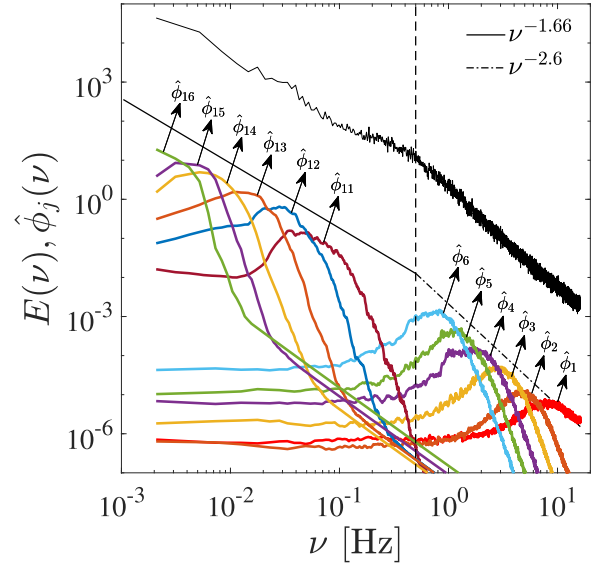

Figure 1. Comparison of Fourier power spectral density $E(\nu)$ (black line) for interval A with the Fourier power spectrum of the different IMFs extracted from the EMD $\hat{\phi}(\nu)$, as a function of frequency ν. The band-like structure of each $\hat{\phi}(\nu)$ shows the dyadic nature of the decomposition. The solid black line indicates $M(\nu) \sim \nu^{-1.66}$ for the inertial range, while the dotted–dashed line indicates $M(\nu) \sim \nu^{-2.6}$ for the scales below the proton gyroscale. The vertical dashed line indicates the position of the proton gyroscale. The gyroscale is the frequency corresponding (via the Taylor hypothesis) to $k\rho_i = 1$, ρ_i being the proton gyroradius.

break scale, where the Fourier spectrum is not described by a power law. Finally, mode $\phi_1(t)$, associated with the smallest timescale, captures the experimental noise embedded in the data sets (Cummings et al. 2004; Wu & Huang 2004), setting the upper limit of the resolvable dynamics and breaking the spectral power-law decay. It is worth mentioning that larger-scale modes with $n > 16$ also exist and are nonvanishing. In particular, modes 17–20 do not present any particular scaling and can be associated with large-scale structures that could act as an energy source for the inertial range.

Once the IMFs have been obtained, the next step of our analysis is to compute the Hilbert transform of each mode

$$\phi_j^\star = \frac{p}{\pi} \int_{-\infty}^{+\infty} \frac{\phi_j(\tau)}{t - \tau} d\tau,$$ (3)

where p is the Cauchy principal value and $\phi_j(t)$ is the jth IMF. The combination of $\phi_j(t)$ and $\phi_j^\star(t)$ defines the analytical signal $\mathcal{Z} = \phi_j + i\phi_j^\star = \mathcal{A}_j(t)e^{i\theta(t)}$, where $\mathcal{A}_j(t)$ is the time-dependent amplitude modulation and $\theta(t)$ is the phase of the mode oscillation (Cohen 1995).

For each mode, the Hilbert spectrum, defined as $H(\nu, t) = \mathcal{A}^2(\nu, t)$ (where $\nu = d\theta/dt$ is the instantaneous frequency), provides energy information in the time–frequency domain. A marginal integration of $H(\nu, t)$ provides the Hilbert marginal spectrum $h(\nu) = T^{-1} \int_0^T H(\nu, t) dt$, defined as the energy density at frequency ν (Huang et al. 1998, 1999). In addition, from the Hilbert spectrum, a joint probability density function $P(\nu, \mathcal{A})$ can be extracted, using the instantaneous frequency ν_j and the amplitude $\mathcal{A}_j$ of the jth IMF. This allows the Hilbert marginal spectrum $h(\nu)$ to be written as

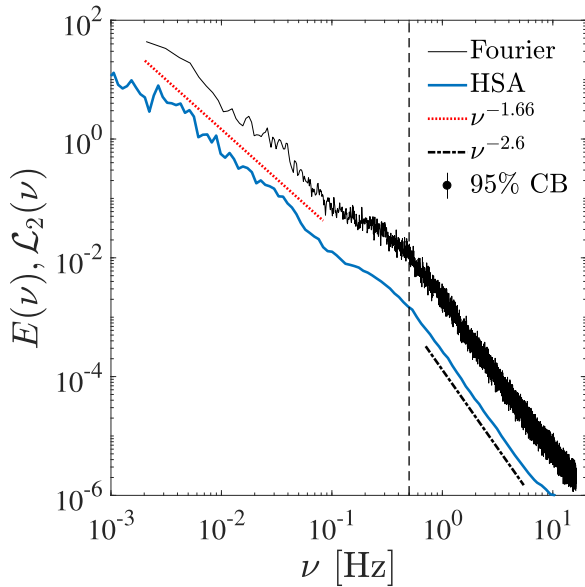$$h(\nu) = \int_0^\infty P(\nu, \mathcal{A}) \mathcal{A}^2 d\mathcal{A},$$ (4)

Figure 2. Comparison of Fourier power spectrum (thin line) with $\mathcal{L}_2(\nu)$ (thick line) for proton density data (interval A). Both methods show a power-law behavior in the inertial range and in the small-scale range, with slopes $\beta \approx 1.66$ and $\beta \approx 2.66$ respectively. The vertical dashed line represents the proton gyroscale. The curves have been vertically shifted for clarity.

which corresponds to a second-order statistical moment (Huang et al. 2008). Equation (4) can be generalized to the arbitrary order $q \geqslant 0$ by defining the ν-dependent qth-order statistical moments

$$\mathcal{L}_q = \int_0^\infty P(\nu, \mathcal{A})\mathcal{A}^q d\mathcal{A}. \qquad (5)$$

In particular, it can be shown that $h(\nu) = \mathcal{L}_2$ represents the analogue of the Fourier spectral energy density (Huang et al. 2008).

In Figure 2, the classical power spectral density $E(\nu)$ evaluated through the Fourier transform is compared with the associated $\mathcal{L}_2(\nu)$, obtained through the HSA. Again, the power-law behavior is present in the same two ranges (i.e., $\mathcal{L}_2(\nu) \sim \nu^{-\beta}$), and the slope β is compatible with the Fourier spectrum: for $\mathcal{L}_2$, power-law fits give $\beta = 1.66 \pm 0.05$ for the inertial range and $\beta = 2.60 \pm 0.01$ for the small-scale range. A better scaling of $\mathcal{L}_2$ can be observed at large scales, where the traditional Fourier spectral density shows a weak amplitude modulation, in the frequency range $\nu \in [10^{-2}, 10^{-1}]$ Hz, comparable with the typical observed size of the ramp–cliff structures (see Figure 7 top panel) (Huang et al. 2010; Carbone et al. 2016a). By analyzing the data, the ramp–cliff duration T has been found in the range $T \in [35 \pm 13, 300 \pm 39]$ s, with an average duration of the order of 71.4 s for the ramps and 27.2 s for the cliffs.

Thanks to the local nature of EMD and HSA, these sources of modulation, as well as the possible effects of ramp–cliff structures, can be constrained, isolating the properties of the cascade from the possible effects of the larger-scale forcing and residual structures (Huang et al. 2010). The scaling properties of the small-scale fluctuations can thus be studied independently of the effect of the intermittent structures arising in the inertial range. Similarly, the inertial-range scaling can be studied independently of the effect of the uncorrelated large-scale fluctuations, often observed as a ν^{-1} spectral
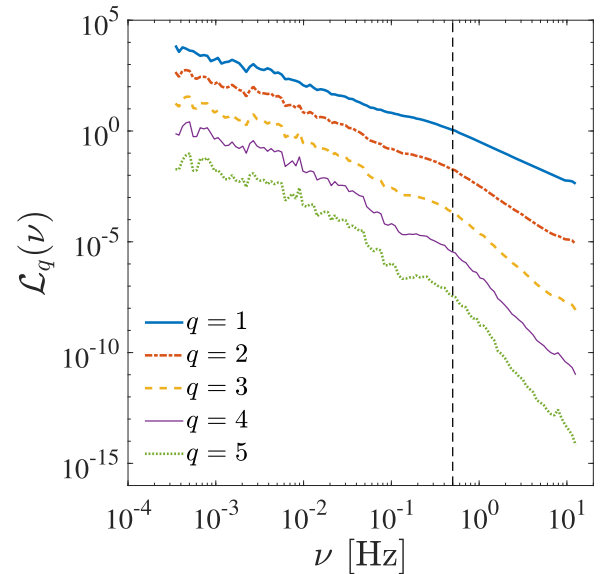

Figure 3. Hilbert spectra $\mathcal{L}_q(\nu)$ for $q = 1, \ldots, 5$, obtained for interval A. The generalized spectra have been shifted for clarity. The dashed line represents the proton gyroscale.

range (Bruno & Carbone 2013). Due to this local nature, HSA allows a better determination of the spectral scaling exponents by mitigating the effects of the instrumental noise and of the larger-scale energy inhomogeneity, both in the inertial range and in the small-scale range. An exhaustive comparison of the results obtained through HSA, detrended fluctuation analysis (DFA), SFs, and wavelet transforms (WT) has been performed in Huang et al. (2011). It was found that both the DFA and WT methods underestimate the scaling exponents, while the SF method may be affected by the presence of ramp–cliff structures or large-scale periodic forcing (Huang et al. 2010; Carbone et al. 2016a).

3. Intermittency Results

As described in Section 2, the generalized second-order Hilbert spectrum has two ranges of power-law scaling $\mathcal{L}_2 \sim \nu^{-\beta}$. In the current *Spektr-R* density data $n_p(t)$, it is possible to extend the measurement of the scaling properties of $\mathcal{L}_q(\nu)$ up to the fifth order. Figure 3 shows $\mathcal{L}_q(\nu)$ for orders $q = 1, \ldots, 5$, obtained from Equation (5) using interval A. The resulting $\mathcal{L}_q(\nu)$ show clear scaling behavior $\mathcal{L}_q(\nu) \sim \nu^{-\beta_q}$ for all q, in the two frequency ranges where the spectra behave as power laws. Classically, the spectral exponent β is linked to the scaling exponent of the second-order SF $S(2) \equiv \langle |x(t + \tau) - x(t)|^2 \rangle \sim \tau^{\zeta(2)}$ (for a generic field of component $x(t)$) via the relation $E(\nu) \sim \nu^{-\beta} \rightarrow \beta = 1 + \zeta(2)$. Extending this relationship to any arbitrary order q, a family of generalized scaling exponents $\xi(q)$ can be introduced through the generalized Hilbert spectra (Huang et al. 2010; Carbone et al. 2016a) as $\xi(q) \equiv \beta_q - 1$. The exponents $\xi(q)$ are the Hilbert analogous of the standard scaling exponents $\zeta(q)$ obtained through the SFs or through the extended self-similarity (ESS) (Benzi et al. 1993; Arneodo et al. 1996). Equation (5) therefore is an alternative to the SF scaling exponents to quantitatively estimate the level of intermittency in the turbulent cascade (Frisch 1995), with the advantage of constraining the effects of noise and large-scale structure. The scaling exponents $\xi(q)$ for the inertial range obtained from the
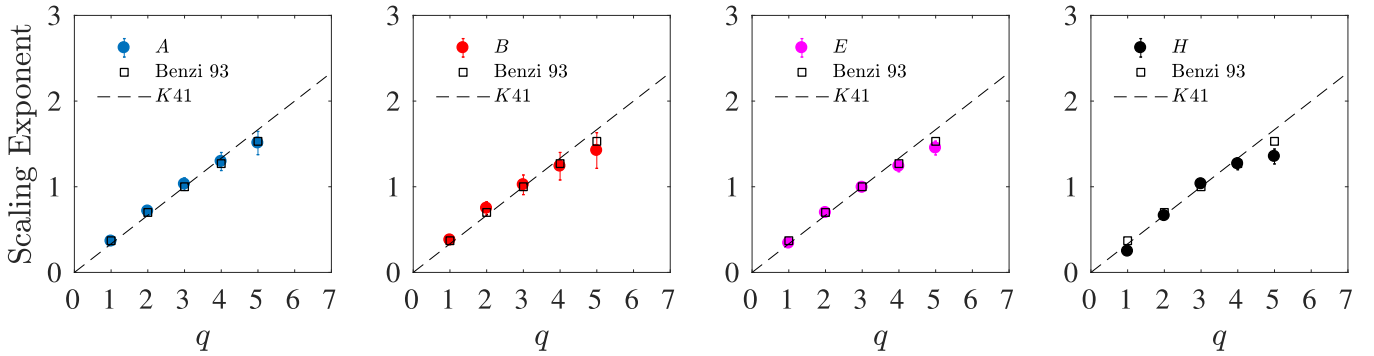
Figure 4. Scaling exponents $\xi(q)$ obtained through the HSA, in the inertial range, for solar wind density in the intervals A, B, E, H (solid symbols); exponents $\zeta(q)$ obtained from velocity fluctuations measured in the inertial range of hydrodynamic turbulence using ESS (open symbols) (Benzi et al. 1993; Arneodo et al. 1996), shown as reference; dashed line: theoretical expectation $q = 1/3$, as estimated from dimensional analysis in the absence of intermittency (Kolmogorov 1941).
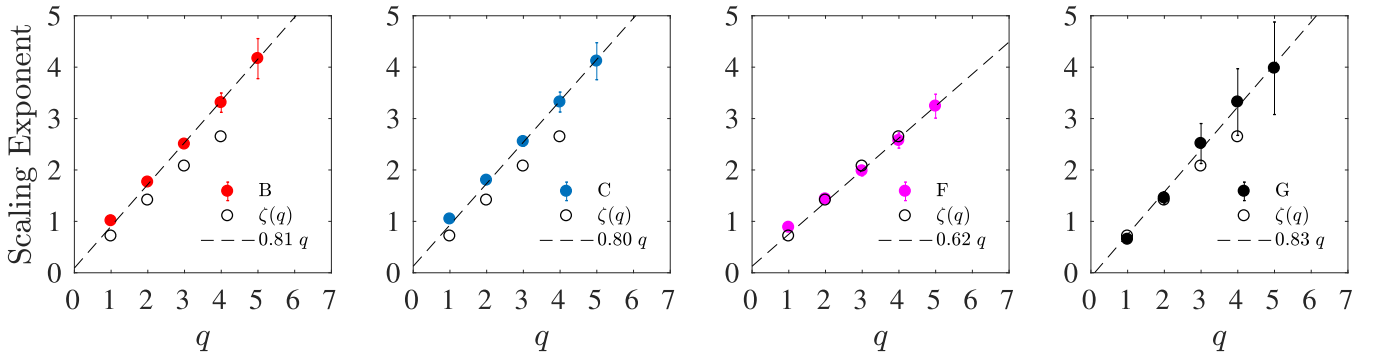

Figure 5. Scaling exponents $\xi(q)$ of the solar wind density, extracted from intervals B, C, F, G (full symbols) at small scale. The dashed lines represent the fitted linear scaling $\xi(q) \simeq 4q/5$ for intervals B, C, G, and $\xi(q) \simeq 3q/5$ for interval F. The open symbols represent the solar wind density scaling exponents $\zeta(q)$ evaluated through the standard Kolmogorov SFs (Chen et al. 2014).

generalized Hilbert spectra $\mathcal{L}_q(\nu)$ are shown in Figure 4. The range of ν selected in order to evaluate the scaling exponent $\xi(q)$ lies in the closed interval $\nu \in [10^{-3}, 9 \times 10^{-2}]$ Hz. Intervals D and G were excluded from the analysis performed in the inertial range, because their limited size does not allow statistical convergence of the high-order moments ($q > 3$). The same figure shows a comparison of $\xi(q)$ with the classical exponents $\zeta(q)$ measured using ESS for the Eulerian velocity fluctuations in experiments on fully developed hydrodynamic turbulence (Benzi et al. 1993; Arneodo et al. 1996). It is easily observed that the departure from the K41 scaling is captured in the solar wind density data, and that the exponents $\xi(q)$ are similar to the standard $\zeta(q)$ obtained in Navier–Stokes fully developed turbulence through the ESS. These are shown as reference, because neither SFs nor the ESS analysis provided power-law scaling for the solar wind density in this range (Chen et al. 2014). The same analysis has been performed on the small-scale range, below the proton gyroscale, in the range $\nu \in [1.5, 9.8]$ Hz. The scaling exponents $\xi(q)$ extracted from the generalized Hilbert spectra $\mathcal{L}_q(\nu)$ are shown in Figure 5. The results are different from the inertial range; in particular, monofractal behavior is found, with $\xi(q)$ presenting a linear scaling compatible with $\xi(q) \sim 4q/5$ for intervals A, B, C, D, G, H, and $\xi(q) \sim 3q/5$ for intervals E, F. As a comparison, in Figure 5, the scaling exponents $\zeta(q)$ obtained through the SF (Chen et al. 2014) in a similar range of scales are reported (the ESS analysis performed in this range gives identical results that are not shown for clarity). The difference between the two exponent sets is evident.

The weak curvature of $\zeta(q)$ could be the remnant signature of the inertial-range structure, which acts as forcing for the dynamics in this range. The EMD–HSA analysis helps to remove these large-scale effects (Huang et al. 2010), to reveal the non-intermittent nature of the small-scale density fluctuations in the solar wind. This result is in contrast with the recent multifractal analysis of the same data (Sorriso-Valvo et al. 2017), where the traditional box-counting measure applied to a surrogate dissipation field suggested a high level of multifractality in the small-scale range. However, the HSA analysis reveals the monofractal nature of the fluctuations, suggesting that the apparent multifractal properties may be the result of residual larger-scale structure (inertial range). A similar monofractal behavior has been found in Consolini et al. (2017) (with different Hurst numbers $\mathcal{H}$), where the linear scaling has been obtained by analyzing the high-resolution *Cluster* magnetic field data set at kinetic scales, and for each magnetic field component.

In order to further check the absence of intermittency, we compare the scaling exponents obtained from $n_p(t)$ with the exponents obtained from the HSA applied to fractional Brownian motion (fBm), with characteristic Hurst numbers $\mathcal{H} = 4/5$ and $\mathcal{H} = 3/5$, respectively. The Hurst number $\mathcal{H}$ describes the long-term memory (persistence) of a process, or the influence that "past" increments have on "future" ones. Values in the range $\mathcal{H} \in (0.5, 1]$ indicate a persistent (long-term memory, correlated) process, while values $\mathcal{H} \in [0, 0.5)$ are associated with anti-persistent (short-term memory, anti-correlated) processes. $\mathcal{H} = 0.5$ indicates a completely uncorrelated process (e.g., a random walk). In the classical
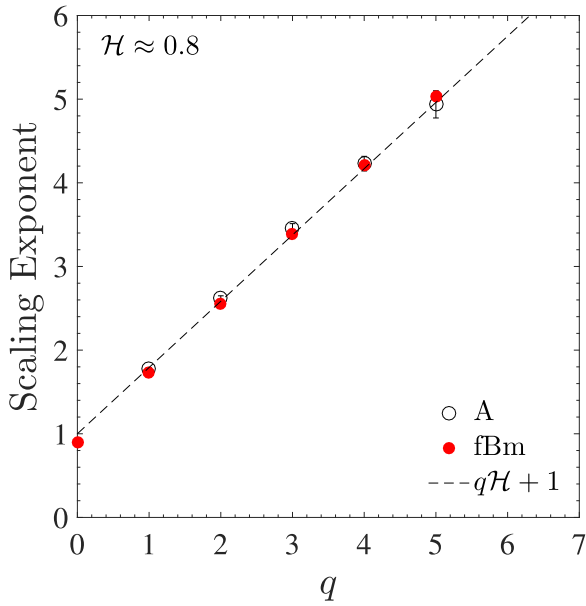
Figure 6. Scaling exponents $\xi(q) + 1$ extracted from interval A (open symbols), and for simulation of fractional Brownian motion with Hurst number $\mathcal{H} = 4/5$. The dashed line represents the theoretical scaling $q\mathcal{H} + 1$.

Kolmogorov theory, in the absence of intermittent corrections, $\zeta(q) = q\mathcal{H}$. By exploiting the relation $\xi(q) = \beta_q - 1 \propto \zeta(q)$ we expect $\xi(q) + 1 \equiv q\mathcal{H} + 1$. The comparison between $\xi(q)$ and the scaling exponents for the fBm ($\mathcal{H} = 4/5$) is given in Figure 6, which shows an excellent agreement supporting the absence of intermittency.

The local Hurst number has also been estimated using an alternative method. The evaluation of local Hurst exponent is a nontrivial issue, for which different approaches have been proposed in the past. One of the most accurate, fast, and simple methods for nonstandard, Gaussian, multi-fractional Brownian motion is the detrending moving average (DMA) technique (Alessio et al. 2002; Carbone et al. 2004; Consolini et al. 2013). Despite its simplicity, this method, based on the analysis of the scaling features of the local standard deviation around a moving average, is more accurate than other methods. The DMA technique consists of evaluating the scaling features of the quantity

$$\sigma_{\mathrm{DMA}}^2(n) = \frac{1}{N_{\max} - n} \sum_{j=n}^{N_{\max}} [f(t) - \bar{f}_n(t)]^2, \qquad (6)$$

where $\bar{f}_n(t)$ represents the average over a moving time window of length n, for different values of the time window in the interval $t_w \in [n, N_{\max}]$. By applying this procedure, the quantity $\sigma_n(t)$ is expected to behave as $\sigma_n(t) \sim n^{\mathcal{H}}$. In order to evaluate $\sigma_n(t)$ from the time series of the solar wind proton density, a moving window of approximately $N_{\max} = 155$ s has been selected.

The detailed temporal evolution of the small-scale $\mathcal{H}_l(t)$ is shown in Figure 7. The top panel shows the density profile $n_p(t)$ for interval A, and the lower panel shows the temporal evolution of the local Hurst number. The results are in good agreement with the Hurst number extracted through the HSA; in particular, a value $\mathcal{H} \approx 0.83 \pm 0.03$ has been found. The maximum percentage error with respect to the empirical value $\mathcal{H} = 0.8$ is of the order of $\Delta\mathcal{H} = 7\%$. The results relative to the other intervals are reported in Table 2.
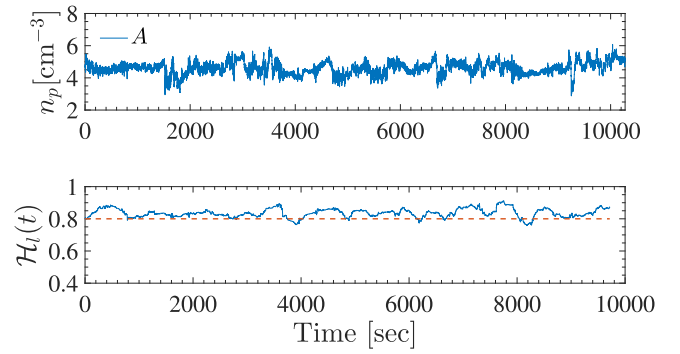

Figure 7. Top panel: the solar wind proton density for interval A. The presence of ramp–cliff structures is visible, for example for times between 4000 and 5000 s. Bottom panel: temporal evolution of the local Hurst number $\mathcal{H}_l(t)$ evaluated through the DMA method (bottom panel), for interval A. The horizontal dashed line represents the expected value $\mathcal{H}_l = 4/5$.

Table 2
Hurst Exponents and Errors

Interval	$\mathcal{H}$	$\langle \mathcal{H}_l(t) \rangle$	$\sigma_{\langle \mathcal{H} \rangle}$	$\Delta\mathcal{H}\%$
A	0.8	0.84	0.03	7.0
B	0.8	0.79	0.05	5.2
C	0.8	0.77	0.06	7.4
D	0.8	0.85	0.05	7.4
E	0.6	0.57	0.09	12.0
F	0.6	0.61	0.09	12.0
G	0.8	0.72	0.06	9.8
H	0.8	0.82	0.07	5.4

Note. For all intervals (Column 1) the table shows the empirical estimate of the Hurst exponent H for the scaling exponents $\xi(q)$ extracted through HSA (Column 2), the average $\langle H_l(t) \rangle$ (Column 3) and the standard deviation $\sigma_{\langle H \rangle}$ (Column 4) of the local Hurst number evaluated through the DMA method, and the maximum percentage error $\Delta H\%$ with respect to the empirical value H.

An example of $\sigma_{\mathrm{DMA}}(n)$, obtained from interval A at $t = 6$ s, is given in Figure 8. At small scales $n \in [0.1, 0.6]$ s, $\sigma_{\mathrm{DMA}}(n)$ shows a good power-law scaling that provides $\mathcal{H} \approx 4/5$, in good agreement with HSA results. The small-scale power-law behavior was robustly observed for all time windows t_w, in all intervals. A second power-law range is also always found in the intermediate range of scales $n \in [1, 3]$ s, around the spectral-break scale, where $\mathcal{L}_2(\nu)$ does not show power-law scaling. It is interesting to observe that in this range the typical exponent for random processes $\mathcal{H}_l \approx 1/2$ is found, exposing the uncorrelated nature of the phenomenon during the transition between the two ranges of scales. For example, some mechanisms could act to decorrelate the intermittent field at the end of the inertial-range cascade, subsequently injecting energy inhomogeneously in the small-scale range. The possibility of understanding the nature of the transition region dynamics using HSA analysis is an important issue that will be studied in depth in a dedicated work. Finally, in the inertial range ($n > 5$ s) there is no evidence of single power-law scaling, in agreement with the multifractal dynamics in this range. After averaging over all running windows, the mean Hurst exponents $\langle \mathcal{H}_l(t) \rangle$ are obtained for each interval. The results are compatible with the fit of the scaling exponents $\xi(q)$, as is visible in Figure 9 where the two sets of values are plotted for the different intervals. Notice that for the HSA exponents the values are consistently closer to the mean values $\mathcal{H} = 4/5$ (and $\mathcal{H} = 3/5$ for intervals E and F). The small discrepancy
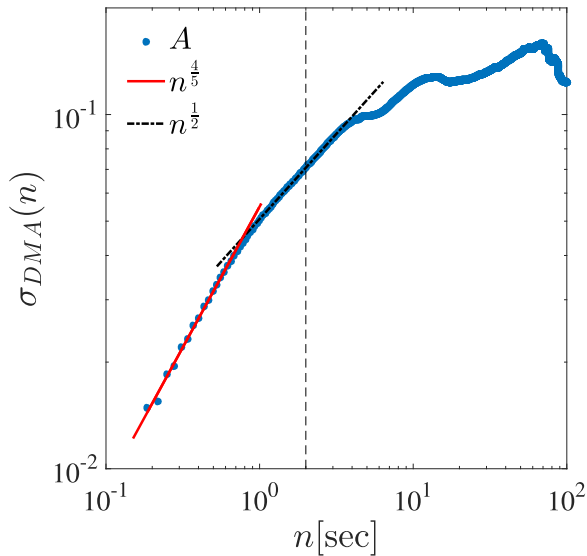
Figure 8. Local Hurst number evaluated through the DMA method. Full symbols: $\sigma_{\mathrm{DMA}}(n)$ as a function of the window length n. Thick red line: range of scales n used to retrieve the small-scale Hurst number $\mathcal{H}_l$. The scaling is in good agreement with the Hurst number evaluated through the HSA. Dotted–dashed line: the secondary range across the proton gyroscale. Vertical dashed line: the proton temporal gyroscale.
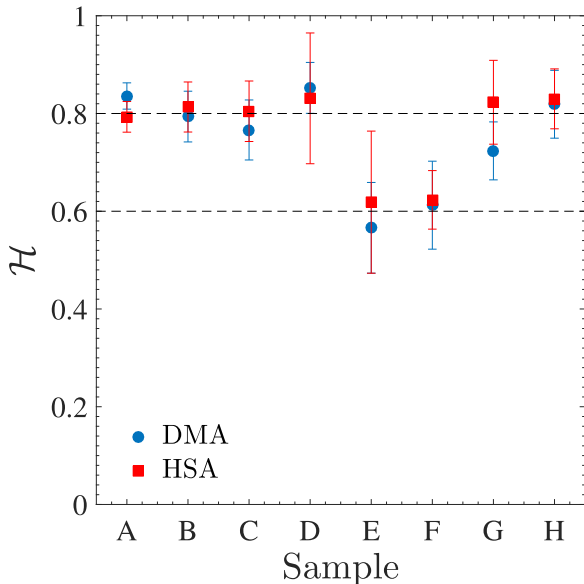

Figure 9. Hurst number $\mathcal{H}$, evaluated through HSA (red squares, the error bars representing the fit parameter uncertainty) and through DMA (blue circles, the error being the standard deviation $\sigma_{\langle \mathcal{H} \rangle}$ from Table 2). The horizontal dashed lines indicate the empirical values $\mathcal{H} = 4/5$ and $\mathcal{H} = 3/5$.

between the two techniques could be attributed to the larger-scale structure, which introduces nonstationarity effects and artificial fluctuations in the scaling exponents, which may mimic multifractality (Sorriso-Valvo et al. 2017). Such effects are removed by HSA, so that the associated local Hurst $\mathcal{H}_l(t)$ values are less affected by the large-scale fluctuations.

4. Conclusions

In an attempt to describe the statistical properties of small-scale turbulence in the solar wind, EMD and the associated arbitrary-order HSA techniques have been applied for the first time to high-frequency density measurements from the

Spektr-R spacecraft. By constructing a family of generalized Hilbert spectra $\mathcal{L}_q(\nu)$, the analogues of the scaling exponents of the SFs have been evaluated from the data. The dyadic filter nature of EMD limits the effects of the large-scale structure (Flandrin et al. 2004; Huang et al. 2010; Carbone et al. 2016a), allowing the identification of a scaling range corresponding to the typical inertial range of solar wind turbulence. Such a scaling range was not observed in this particular data set using the traditional higher-order moments of the fluctuations. The exponents $\xi(q)$ estimated through HSA fully capture the anomalous scaling properties related to intermittency, exposing the multifractal nature of the inertial-range turbulent cascade (Frisch 1995). In particular, they are found to be in good agreement with the classical exponents observed in Eulerian velocity fluctuations in isotropic fluid turbulence (Benzi et al. 1993; Arneodo et al. 1996).

The high resolution of the *Spektr-R* density measurements also allows the scaling properties of fluctuations below the proton gyroscale to be investigated, where the presence of intermittency is still debated (Alexandrova et al. 2013; Chen et al. 2014; Sorriso-Valvo et al. 2017). In this range, the scaling exponents obtained through HSA show a linear dependence on the order $\xi(q) \sim q\mathcal{H}$. This suggests that the system loses its multiscaling properties and converges to a non-intermittent, monofractal behavior. Two values of the Hurst number $\mathcal{H} \approx 3/5, \, 4/5$ have been found in the eight intervals under study, indicating a persistent process (long-term memory). The monofractal nature of the small-scale fluctuations has been confirmed through a comparison with the HSA analysis of fractional Brownian motion with the same Hurst number. Furthermore, the Hurst number has also been estimated for all intervals using the DMA method. The values obtained with DMA are in good agreement with the HSA results, supporting the validity of the results.

The origin of difference between the intermittency properties of the inertial- and kinetic-range turbulence in the solar wind, also suggested in some previous works (Kiyani et al. 2009; Chen et al. 2014), remains an important unanswered question. The results in this paper confirm this difference, providing a more accurate measure of the scaling exponents and placing a tighter constraint on the statistical properties of the density fluctuations. Possible reasons for the difference include the increasing importance of wave–particle interactions in the kinetic range and an inherent difference in the form of the nonlinear interactions of the cascade. The current measurements provide an important constraint on future models of kinetic turbulence.

The results presented in this paper show that the scaling properties of solar wind fluctuations need a careful analysis, and that the larger-scale fluctuations may affect the statistical properties of the scales under study. The HSA analysis seems to be able to reduce such an effect, providing a more accurate measure of the scaling properties of the field.

ORCID iDs

Francesco Carbone ⬤ https://orcid.org/0000-0002-3559-5273
Luca Sorriso-Valvo ⬤ https://orcid.org/0000-0002-5981-7758
Tommaso Alberti ⬤ https://orcid.org/0000-0001-6096-0220
Fabio Lepreti ⬤ https://orcid.org/0000-0001-5196-2013
Zdenek Němeček ⬤ https://orcid.org/0000-0002-8160-3051
Jana Šafránková ⬤ https://orcid.org/0000-0003-4178-5206

References

Alberti, T., Consolini, G., Lepreti, F., et al. 2017, JGRA, 122, 4266
Alessio, E., Carbone, A., Castelli, G., & Frappietro, V. 2002, EPJB, 27, 197
Alexandrova, O., Carbone, V., Veltri, P., & Sorriso-Valvo, L. 2008, ApJ, 674, 1153
Alexandrova, O., Chen, C. H. K., Sorriso-Valvo, L., Horbury, T. S., & Bale, S. D. 2013, SSRv, 178, 101
Arneodo, A., Baudet, C., Belin, F., et al. 1996, EPL, 34, 411
Benzi, R., Ciliberto, S., Tripiccione, R., et al. 1993, PhRvE, 48, R29
Boldyrev, S. 2006, PhRvL, 96, 115002
Bruno, R., & Carbone, V. 2013, LRSP, 10, 2
Bruno, R., Telloni, D., Primavera, L., et al. 2014, ApJ, 786, 53
Carbone, A., Castelli, G., & Stanley, H. 2004, PhyA, 344, 267
Carbone, F., Gencarelli, C. N., & Hedgecock, I. M. 2016a, PhRvE, 94, 063101
Carbone, F., Landis, M. S., Gencarelli, C. N., et al. 2016b, GeoRL, 43, 7751
Celani, A., Lanotte, A., Mazzino, A., & Vergassola, M. 2000, PhRvL, 84, 2385
Chen, C. H. K. 2016, JPlPh, 82, 535820602
Chen, C. H. K., Bale, S. D., Salem, C., & Mozer, F. S. 2011, ApJL, 737, L41
Chen, C. H. K., Sorriso-Valvo, L., Šafránková, J., & Němeček, Z. 2014, ApJL, 789, L8
Cohen, L. 1995, Time–Frequency Analysis (Englewood Cliffs, NJ: Prentice-Hall)
Consolini, G., Alberti, T., Yordanova, E., Marcucci, M. F., & Echim, M. 2017, J. Phys. Conf. Ser., 900, 012003
Consolini, G., De Marco, R., & De Michelis, P. 2013, NPGeo, 20, 455
Cummings, D. A., Irizarry, R. A., Huang, N. E., et al. 2004, Natur, 427, 344
Flandrin, P. 1999, Time–Frequency/Time-Scale Analysis (1st ed.; New York: Academic)
Flandrin, P., Rilling, G., & Goncalves, P. 2004, ISPL, 11, 112

Frisch, U. (ed.) 1995, Turbulence: the Legacy of A. N. Kolmogorov (Cambridge: Cambridge Univ. Press)
Goldreich, P., & Sridhar, S. 1995, ApJ, 438, 763
He, J., Wang, L., Tu, C., Marsch, E., & Zong, Q. 2015, ApJL, 800, L31
Hnat, B., Chapman, S. C., & Rowlands, G. 2003, PhRvE, 67, 056404
Huang, N. E., & Shen, S. S. P. (ed.) 2005, The Hilbert–Huang Transform and Its Applications (Singapore: World Scientific)
Huang, N. E., Shen, Z., Long, S. R., et al. 1998, RSPSA, 454, 903
Huang, N. E., Shen, Z., & Long, S. R. 1999, AnRFM, 31, 417
Huang, Y. X., Schmitt, F. G., Hermand, J.-P., et al. 2011, PhRvE, 84, 016208
Huang, Y. X., Schmitt, F. G., Lu, Z. M., et al. 2010, PhRvE, 82, 026319
Huang, Y. X., Schmitt, F. G., Lu, Z. M., & Liu, Y. L. 2008, EPL, 84, 40010
Iroshnikov, P. S. 1964, SvA, 7, 566
Kiyani, K. H., Chapman, S. C., Khotyaintsev, Y. V., Dunlop, M. W., & Sahraoui, F. 2009, PhRvL, 103, 075006
Kolmogorov, A. N. 1941, DoSSR, 36, 301
Kraichnan, R. H. 1965, PhFl, 8, 1385
Leamon, R. J., Smith, C. W., Ness, N. F., Matthaeus, W. H., & Wong, H. K. 1998, JGRA, 103, 4775
Liu, Q., Fujita, T., Watanabe, M., & Mitani, Y. 2012, in IFAC Proc. 45, 8th Power Plant and Power System Control Symp. (New york: Elsevier), 144
Marsch, E., & Tu, C.-Y. 1997, NPGeo, 4, 101
Šafránková, J., Němeček, Z., Němec, F., et al. 2015, ApJ, 803, 107
Šafránková, J., Němeček, Z., Přech, L., et al. 2013a, SSRv, 175, 165
Šafránková, J., Němeček, Z. v., Přech, L., & Zastenker, G. N. 2013b, PhRvL, 110, 025004
Salisbury, J. I., & Wimbush, M. 2002, NPGeo, 9, 341
Servidio, S., Osman, K. T., Valentini, F., et al. 2014, ApJL, 781, L27
Servidio, S., Valentini, F., Califano, F., & Veltri, P. 2012, PhRvL, 108, 045001
Shraiman, B. I., & Siggia, E. D. 2000, Natur, 405, 639
Sorriso-Valvo, L., Carbone, F., Leonardis, E., et al. 2017, AdSpR, 59, 1642
Sorriso-Valvo, L., Carbone, V., Veltri, P., Consolini, G., & Bruno, R. 1999, GeoRL, 26, 1801
Sreenivasan, K. R. 1991, RSPSA, 434, 165
Vecchio, A., Anzidei, M., & Carbone, V. 2014, JGeo, 79, 39
Warhaft, Z. 2000, AnRFM, 32, 203
Wroblewski, D. E., Coté, O. R., Hacker, J. M., & Dobosy, R. J. 2007, JAtS, 64, 2521
Wu, Z., & Huang, N. E. 2004, RSPSA, 460, 1597
Yeung, P. K., Brasseur, J. G., & Wang, Q. 1995, JFM, 283, 4395